ADVANCED FUNCTIONAL MATERIALS
www.afm-journal.de

Materials Views
www.MaterialsViews.com

Anti-Ferromagnet Controlled Tunneling Magnetoresistance

Yuyan Wang, Cheng Song, Guangyue Wang, Jinghui Miao, Fei Zeng, and Feng Pan**

The requirement for high-density memory integration advances the development of newly structured spintronic devices, which have reduced stray fields and are insensitive to magnetic field perturbations. This could be visualized in magnetic tunnel junctions incorporating anti-ferromagnetic instead of ferromagnetic electrodes. Here, room-temperature anti-ferromangnet (AFM)-controlled tunneling anisotropic magnetoresistance in a novel perpendicular junction is reported, where the IrMn AFM stays immediately at both sides of AlO_x tunnel barrier as the functional layers. Bi-stable resistance states governed by the relative arrangement of uncompensated anti-ferromagnetic IrMn moments are obtained here, rather than the traditional spin-valve signal observed in ferromagnet-based tunnel junctions. The experimental observation of room-temperature tunneling magnetoresistance controlled directly by AFM is practically significant and may pave the way for new-generation memories based on AFM spintronics.

1. Introduction

The discoveries of giant magnetoresistance (GMR) in 1988 and the following tunneling magnetoresistance (TMR) establish the basis for current spintronic applications, which center on magnetic storage and sensing.[1–5] So far, the GMR- and TMR-based devices typically feature a trilayer system with two ferromagnets (FM) sandwiching a non-magnetic metal or insulating layer.[1,6] Unfortunately, the existence of ferromagnetic stray fields and the sensitivity of FM to magnetic field perturbations pose great obstacles for high-density memory integration.[1] To eliminate these unfavorable factors, applications of anti-ferromagnets (AFM) in spintronics are attracting increasing interest much beyond their current passive role as pinning layers. The rigidity to external magnetic fields and the absence of stray fields make AFM particularly favorable for ultrafast and ultrahigh-density spintronics.[7–9] Early studies that achieved spin-dependent tunneling with AFM electrodes were carried out in scanning tunneling microscope using the vacuum as the tunneling gap.[10,11] Recently, spin-transfer torques[12] and magnetoresistance effects[13] have been theoretically predicted and experimentally confirmed in AFM memory resistors[14,15] and AFM-based tunnel junctions with only a single IrMn layer adjacent to the barrier.[14,16,17] The manipulation of AFM moments via an exchange-coupled FM and the detection of tunneling anisotropic magnetoresistance (TAMR) have been realized at room temperature.[17] Nevertheless, the spin signals arise from the magnetic anisotropy of tunneling density of states in a single magnetic electrode on the basis of exchange coupling, and the interaction between the non-magnetic top electrodes and AFM electrodes makes no sense for TAMR.[18] The tunneling magnetoresistance between two AFMs (bi-AFM TAMR) across a tunnel barrier is still in a realm that lacks experimental insight and in-depth investigation. It would be technically significant if the AFM moments could be freely manipulated on both sides of the barrier, thus achieving the preferable functionality for miniaturized memories that cannot be obtained with FM.

There are two crucial factors for realizing bi-AFM TAMR: the independent reversal of the two AFM layers in different response to the stimulus and the immediate interaction between the moments in AFM across the barrier. Here, Co/Pt multilayers are chosen as a supporting material to trigger the rotation of IrMn moments because of their superior thermal tolerance as well as perpendicular magnetic anisotropy (PMA), which can be easily tailored by varying the thickness of Co.[19–22] The experiments reported demonstrate a novel junction IrMn/AlO_x/IrMn where AFM-controlled room-temperature TAMR is achieved and is governed by the relative arrangement of the uncompensated AFM moments separated by the AlO_x barrier.

2. Results and Discussion

Multilayers of $[Pt(1)/Co(0.5)]_5$/IrMn(t)/AlO_x(2)/IrMn(t)/$[Co(0.3)/Pt(1)]_5$ (unit in nanometers) with different IrMn thicknesses (t) of 2 nm, 6 nm, 10 nm and 20 nm were grown by magnetron sputtering at room temperature. Different thicknesses of Co in the top Co/Pt layer (Co 0.3 nm) and the bottom layer (Co 0.5nm) are adopted to tailor the coercivity of the Co/Pt multilayers. The PMA of the multilayers with different t at 300 K is characterized by magnetic hysteresis loops, as shown in the left column of **Figure 1** (Figure S1 in the Supporting Information). Remarkably, there exists a platform separating two different coercivities (H_C) in each magnetization loop under out-of-plane fields (H). The larger H_C originates from the bottom [Pt/Co(0.5)]/IrMn and the smaller H_C corresponds

Y. Y. Wang, Dr. C. Song, G. Y. Wang, J. H. Miao, Dr. F. Zeng, Prof. F. Pan
Key Laboratory of Advanced Materials (MOE)
School of Materials Science and Engineering
Tsinghua University
Beijing 100084, China
E-mail: songcheng@mail.tsinghua.edu.cn; panf@mail.tsinghua.edu.cn

DOI: 10.1002/adfm.201401659

© 2014 WILEY-VCH Verlag GmbH & Co. KGaA, Weinheim

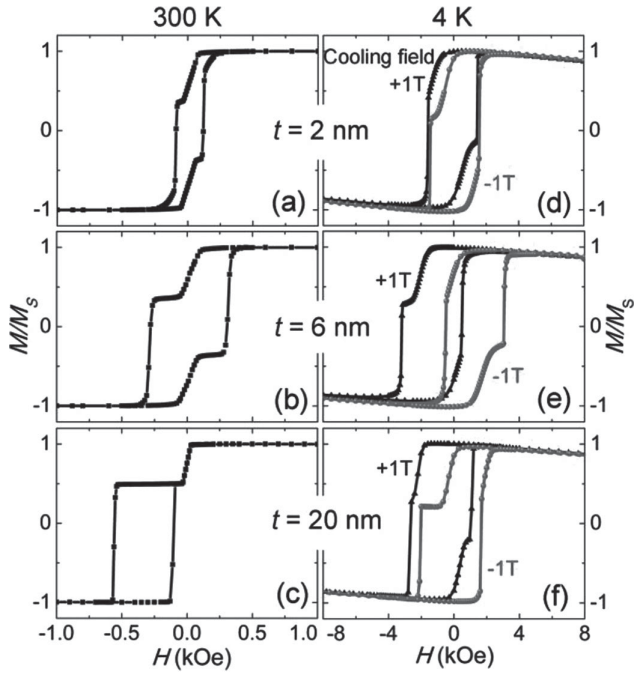

Figure 1. Normalized magnetization loops of the stack structure with a) 2 nm IrMn, b) 6 nm IrMn, and c) 20 nm IrMn at 300 K. Normalized field-cooled magnetization loops measured at 4 K with cooling fields of +10 kOe (triangles) and –10 kOe (circles) of the stack structures with d) 2 nm IrMn, e) 6 nm IrMn, and f) 20 nm IrMn.

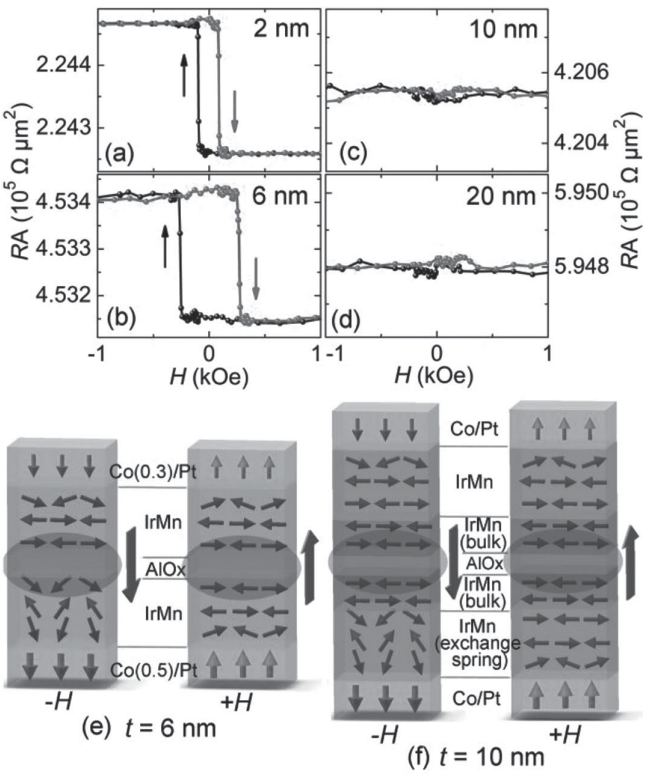

Figure 2. Magnetoresistance acquired by sweeping vertical *H* at 300 K for the junctions with different *t*: a) 2 nm, b) 6 nm, c) 10 nm, and d) 20 nm. Schematics of the moment arrangements in the junctions at $-H$ and $+H$ are shown in e) 6 nm IrMn and f) 10 nm IrMn. Arrows in the cubic represent the IrMn moments and Co/Pt moments. The black arrows denote the directions of external *H*.

to the magnetically softer IrMn/[Co(0.3)/Pt] top layer. Besides, a strong PMA of the bottom Co/Pt layer with (111)-oriented texture is induced by the Pt buffer layer,[23] while the predeposition of IrMn damages the fcc texture of the top Co/Pt, resulting in a weaker PMA.[24] Accordingly, a weaker coupling between the top Co/Pt and IrMn is obtained, leading to a subtle moment rotation within IrMn. For $t = 6$ nm, the corresponding perpendicular anisotropy energy is estimated to be $K_{u1} \approx 4.55 \times 10^6$ erg cm^{-3} and $K_{u2} \approx 3.25 \times 10^5$ erg cm^{-3}, respectively.[25] To verify the perpendicular exchange coupling between Co/Pt and IrMn AFM, each sample was measured at 4 K with the cooling *H* of ±10 kOe (right column of Figure 1). The shift of the magnetization loops indicates a strong exchange coupling which enables the effective manipulation of IrMn moments through Co/Pt magnetization. Clearly, the separation of H_C as well as the different PMA for the top and bottom coupling layer is successfully achieved, which could trigger different alignment of IrMn moments in the same magnetic field, providing a fundamental basis for the generation of bi-AFM TAMR.

We next focus on the magnetoresistance of the tunnel junctions controlled by IrMn AFM. **Figure 2**a–d present the resistance-area (RA) product measured with vertical *H* at 300 K as $t = 2$ nm, 6 nm, 10 nm, and 20 nm, respectively. Hysteresis windows with stable low-resistance states (LRS) at $+H$ and high-resistance states (HRS) at $-H$ are clearly recognizable in Figure 2a,b, where the magnitude of the reversal field coincides with the H_C of the bottom [Pt/Co]/IrMn layer for both of the samples with 2 nm- and 6 nm-thick IrMn, as shown in Figure 1. The extraordinary TAMR with only one sharp reversal during sweeping *H*, different from the traditional spin-valve-like signals in FM-based tunnel junctions, is ascribed to the changes in the density of states when IrMn moments rotate with respect to the crystallographic directions.[16,17] This rotation is obtained by the exchange-spring effect, and the two H_C at both sides of the barrier trigger the rotations at different instances.

The graphics in Figure 2e depict the moment arrangements in the whole junctions and illustrate the generation of HRS and LRS for $t = 6$ nm, the optimal thickness for obtaining a combination of strong perpendicular exchange coupling and TAMR. In general, IrMn anti-ferromagnetic layer exhibits an in-plane easy direction[26]. Taking the case of the bottom [Pt/Co]/IrMn coupling layer firstly, the bulk moments in IrMn are aligned in-plane when vertical $+H$ is applied (in-plane arrows in Figure 2e), but at $-H$ there is a partial rotation of the IrMn moments which is triggered by the sharp reversal of Co/Pt moments (out-of-plane arrows).[17] This observed asymmetry between the two states (at $+H$ and $-H$) could be attributed to the original downward component of the interfacial IrMn moments at the interface of Co/Pt and IrMn, which is an imprint of the domain pattern of the as-deposited Co/Pt.[27] Due to this initial tilt, IrMn spins prefer to rotate downward at $-H$ while align almost in-plane at $+H$. It is worth pointing out that the entire IrMn layer forms an exchange-spring for *t* smaller than the domain-wall width (≈7.8 nm).[17,28] Consequently, the uncompensated interfacial spins of IrMn adjacent to AlO_x barrier tilt from in-plane to out-of-plane direction as the field sweeps from $+H$ to

© 2014 WILEY-VCH Verlag GmbH & Co. KGaA, Weinheim

–*H*. Note that the strong PMA at the interface of bottom [Pt/Co]/IrMn is responsible for driving the rotation of the whole IrMn exchange-spring.

In the magnetically softer IrMn/[Co/Pt] top layers, the Co/Pt moments undergo a gentle reversal from the upward to the downward direction (highlighted by the thin arrows in top Co/Pt). In this scenario, the moments in the top IrMn adjacent to AlO_x barrier almost align in-plane during sweeping *H*, except for the slightly canted IrMn moments at the interface of IrMn/[Co/Pt] due to exchange coupling. Compared with the high K_u of the bottom FM, the IrMn moments are hardly rotated by the top Co/Pt with weak PMA, resulting in a weak or negligible exchange spring in IrMn. To sum up, the uncompensated in-plane moments adjacent to AlO_x barrier in the top and bottom IrMn align parallel at +*H* and produce the LRS in Figure 2b. However, the angle between the uncompensated interfacial IrMn moments (marked in Figure 2e) generates the HRS at –*H*,[29,30] closely related to the formation of the IrMn exchange-spring in the bottom layer. Because of the relative immobility of the top IrMn moments during sweeping *H*, the only one sharp resistance transition in Figure 2b is attributed to the rotation of the bottom IrMn moments driven by Co/Pt, corresponding to the H_C of the bottom [Pt/Co]/IrMn layer (Figure 1b). When *t* decreases to 2 nm, the observed TAMR in Figure 2a could be easily interpreted as a shorter exchange-spring in IrMn remains to change the relative alignment of IrMn moments adjacent to AlO_x barrier.

However, the magnetoresistance signals vanish in samples with *t* = 10 nm and 20 nm (Figure 2c and d). It is worth mentioning that the thick IrMn layer (10 nm or 20 nm) could be divided into two parts (Figure 2f): the exchange-spring (≈7.8 nm) and the bulk.[17,31] The exchange-spring is formed in the vicinity of Co/Pt FM, while the bulk part is formed close to AlO_x. Even though the exchange-spring could be rotated by Co/Pt magnetization, the uncompensated moments in bulk IrMn adjacent to AlO_x align persistently in-plane (Figure 2f). As a result, the relative orientation of the uncompensated AFM moments in top and bottom IrMn remains parallel during sweeping *H*, leading to the constant resistance (Figure 2c,d). These *t*-dependent TAMR signals confirm the crucial role of the interfacial IrMn moments separated by AlO_x. Note that both top and bottom IrMn thicknesses are changed simultaneously in the present case. In fact, because of the relatively stationary moments in the top IrMn which are scarcely rotated by the top Co/Pt with weak PMA, the TAMR is insensitive to the top IrMn when only its thickness is varied. Particularly, when the top IrMn layer is removed, the interactions between the top Co/Pt FM and bottom IrMn AFM through AlO_x barrier give rise to the HRS/LRS in the magnetoresistance curves,[30] in contrast to negligible signals for the case of removing the bottom IrMn (Figure S2, Supporting Information). As is generally known, traditional FM-based tunnel junctions with sandwich structure generate spin-valve effect, where the two reversals between LRS and HRS reflect specific correlation with the magnetizations of top and bottom FM electrodes.[1,6] In our case, the only one reversal of resistance verifies that the bi-AFM TAMR is dominated by the relative arrangement of IrMn moments, rather than the Co/Pt FM.

Further evidence for the partial rotation of IrMn moments is provided by the Mn *L*-edge X-ray magnetic linear dichroism

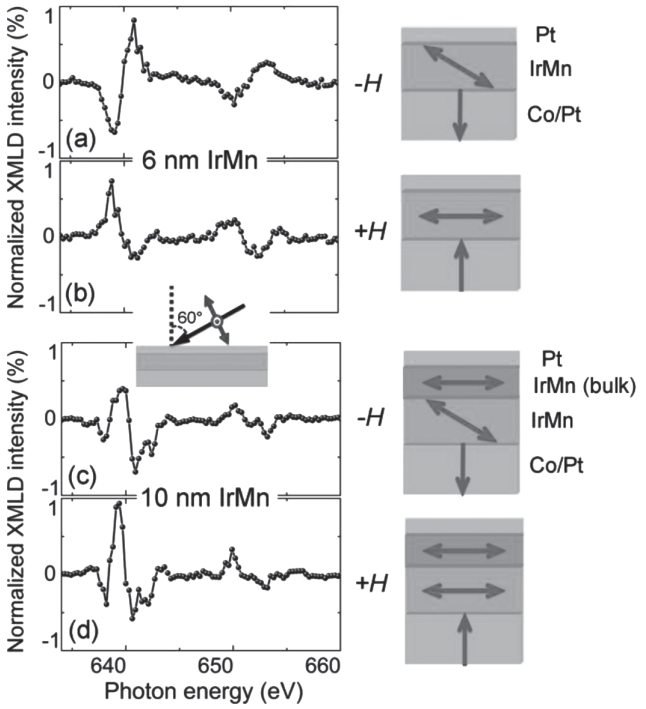

Figure 3. Mn *L*-edge XMLD difference in absorption intensities for the in-plane and out-of-plane linear polarization vectors *E*: a) 6 nm IrMn at –*H*, b) 6 nm IrMn at +*H*, c) 10 nm IrMn at –*H*, and d) 10 nm IrMn at +*H*. Right insets: schematic drawing of the moment arrangements in [Pt/Co]/IrMn corresponding to each figure.

(XMLD) experiments, characterized by different absorption of light with its linear polarization vector *E* orientated parallel or perpendicular to the spin axis of IrMn.[15,31,32] Multilayers of substrate/[Pt(1)/Co(0.5)]$_5$/IrMn/Pt(2) with 6 nm- and 10 nm-thick IrMn were prepared since the detection depth is less than 5 nm. The linear polarization was rotated by 90° to obtain the in-plane and out-of-plane (60° from the surface) *E* (see the left inset of **Figure 3**). Then XMLD differences in absorption intensities ($I_{\text{in-plane E}}$–$I_{\text{out-of-plane E}}$) of each sample at the two remanent states after magnetization (+2 kOe and –2 kOe) are plotted in Figure 3. For the sample with 6 nm-thick IrMn, the opposite sign of the XMLD spectra (Figure 3a,b) confirms that the IrMn moments in the two states (after +*H* and –*H*) are rotated by an angle with respect to each other.[15] In contrast, for 10 nm IrMn quite similar XMLD spectra are detected at opposite *H* (Figure 3c and d), indicating the same arrangement of IrMn moments. As is known, the signals for the thick IrMn are largely contributed by the moments in bulk IrMn far from the [Pt/Co]/IrMn interface, which are aligned in-plane and hardly rotated by Co/Pt when we take the domain wall width of ≈7.8 nm into account (insets of Figure 3c,d). Thus we can conclude that for the sample with 6 nm-thick IrMn, the moments in the exchange-spring are in-plane at +*H*, according to the similar XMLD spectra between Figure 3b–d. Nevertheless, the opposite signals observed in Figure 3a indicate a partial rotation of IrMn moments towards the out-of-plane direction (inset of Figure 3a). These elemental specific XMLD results confirm the twisted IrMn moments in the bottom [Pt/Co]/IrMn coupling layer, thus supporting the graphics of moment arrangements in Figure 2.

© 2014 WILEY-VCH Verlag GmbH & Co. KGaA, Weinheim

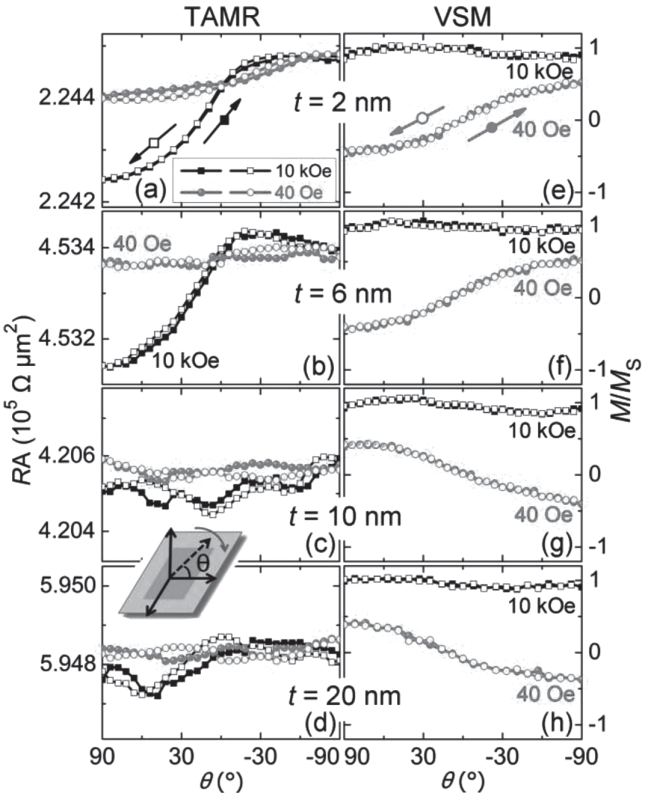

Figure 4. a–d) The effect of rotating junctions with different t on resistance in fixed H of 40 Oe (circles) and 10 kOe (squares). e–h) The magnetization of the stack structures as a function of out-of-plane rotation. The inset: the sample was rotated first from $\theta = 90°$ to $\theta = -90°$ (filled symbols) and then backwards (open symbols). All data were recorded at 300 K.

We have explored the resistance and magnetization as a function of out-of-plane rotation (θ) to explicit the AFM origin of TAMR. The samples with different t were rotated from a vertical field ($\theta = 90°$) to an in-plane field ($\theta = 0°$), and continue to $\theta = -90°$, finally backwards to $\theta = 90°$. Both the TAMR and vibrating sample magnetometer (VSM) measurements were recorded by setting two opposite extreme fields of 40 Oe (circles) and 10 kOe (squares). At first glance, the RA product as a function of θ is closely related to t (left column of **Figure 4**). During rotating the device in a 40 Oe field, the RA product with $t = 2$ nm increases gradually (circles in Figure 4a), indicating a slight rotation of the bottom IrMn moments. However, this low field is insufficient to trigger an exchange-spring action on the 6 nm-thick IrMn,[17,33] without breaking the parallel alignment between the uncompensated IrMn moments, which brings about a nearly constant RA signal (Figure 4b). Thus the varied tendencies of angle-dependent RA between the samples with 2 nm- and 6 nm-thick IrMn verify the crucial role of anti-ferromagnetic moments in the observed TAMR. When a 10 kOe high field is applied, the resistance changes from a LRS to a HRS with θ rotating from 90° to –90°, as a result of the relative arrangement between uncompensated IrMn moments (squares in Figure 4a,b). In contrast to the tunneling transport by IrMn, the VSM signal is sensitive to Co/Pt. The magnetization rotates with the sample at 40 Oe, far below the H_C of the bottom coupling layer (circles in Figure 4e,f). While it increases to be saturated at 10 kOe, the magnetization keeps its orientation parallel to the external fields at all angles, generating a constant VSM signal. This clear distinction between the TAMR and VSM measurements confirms the AFM-controlled origin of the detected TAMR signals, differing from the FM-dominant TMR.

The situation changes dramatically when t increases to 10 nm and 20 nm. From the curves in Figure 4c,d, we note that the RA signals present negligible changes, except for noises. As discussed in Figure 2f, the relative orientation of the uncompensated AFM moments in the top and bottom IrMn remains parallel during the rotation, leading to the constant resistance. In addition, Figure 4g,h display the magnetization features of Co/Pt FM in the stack with 10 nm- and 20 nm-thick IrMn, which are relevant to their corresponding magnetization features (Figure S3, Supporting Information).

It is quite natural to remind us of the TAMR effect in the junction comprising of only one AFM electrode (referred to as one-AFM TAMR), which is intimately related to the anisotropy of tunneling density of states on one side of the barrier, where the whole exchange-spring of AFM works.[16,17] Nevertheless the observed bi-AFM TAMR here and the one-AFM TAMR effect are not completely the same. In spite of the similar origins of the TAMR effect based on the changes of the density of states in IrMn, the relative arrangement of the moments in two AFM layers also greatly contributes to the transport properties in the case of bi-AFM TAMR, proved by the following two aspects. Firstly, a LRS is detected because of the parallel relationship between the IrMn moments at the initial $+H$ in the bi-AFM TAMR, contrary to the HRS in the [Pt/Co]/IrMn/AlOx/Pt junctions at $+H$ which is related to the angle between in-plane IrMn moments and upward Co/Pt moments (Figure S4, Supporting Information). Secondly, the room-temperature one-AFM TAMR effect could only be detected as IrMn is thicker than 4 nm in order to ensure the stability of AFM moments, even though the magnitude drops gradually from 8 nm to 20 nm (Figure S5, Supporting Information). It is interesting that bi-AFM TAMR cannot be detected when t is larger than the length of a whole exchange-spring (such as $t = 10$ nm and 20 nm), but a recognizable signal appears in the sample with 2 nm-thick IrMn (Figure S6, Supporting Information). It confirms that the bi-AFM TAMR in the present case is closely related to the interactions between two IrMn layers adjacent to AlO_x, not merely the anisotropy of tunneling density of states in IrMn on one side of the barrier. Combining the magnetization and magnetoresistance measurements, we can conclude that the bi-AFM TAMR reported here is not only essentially different from the ordinary TMR based on FM, but also not exactly the same with the previous one-AFM TAMR. Admittedly, further optimization of the tunnel barrier and interfaces in the present junctions is required to increase the ratio of TAMR to a magnitude comparable with TMR based on FM.

3. Conclusions

In summary, we have demonstrated a room-temperature tunneling magnetoresistance effect in anti-ferromagnet-based tunnel junctions. In contrast to the traditional ferromagnetic

© 2014 WILEY-VCH Verlag GmbH & Co. KGaA, Weinheim

tunnel junctions, a unique structure is designed in our work to place two IrMn layers on both sides of AlO_x barrier. The neighboring Co/Pt FM electrodes with distinct PMA are utilized to control the IrMn moments through exchange coupling. In particular, bi-stable resistance states (LRS/HRS) are detected as a result of the relative arrangement of IrMn moments, associated with the partial rotation of the exchange-spring. The elemental specific XMLD spectra and TAMR measurements as a function of IrMn thicknesses and rotating devices confirm the dominant role of uncompensated interfacial IrMn moments separated by the barrier. We propose a new paradigm for AFM-controlled transport if the moments in the two AFM layers could be independently controlled by spin current, electric field or strain engineering, with the absence of FM in the whole devices. Because of the superior features of AFM such as negligible stray fields and insensitivity to strong magnetic fields compared to FM, the utilization of AFM in tunnel junctions will be a cornerstone for exploring the ultrafast and high-density spintronic devices.

4. Experimental Section

Multilayers of $[Pt(1)/Co(0.5)]_5/IrMn(t)/AlO_x(2)/IrMn(t)/[Co(0.3)/Pt(1)]_5$ (unit in nanometers) were grown on Si/SiO_2 substrates with a 15 nm-thick Pt buffer layer. The multilayers were patterned into rectangle-shaped junctions of dimensions 20×12 μm^2, using photolithography and ion milling. X-ray diffraction was used to study the crystalline texture of the multilayers, showing a Co/Pt (111) preferred orientation. The magnetization properties were carried out in a superconducting quantum interference device by Quantum Design. Measurements with fields up to 10 kOe were performed in a vibrating sample magnetometer. The tunneling magnetoresistance was measured by a four-point contact geometry with a bias of 100 μA at 300 K, using the Physical Property Measurement System by Quantum Design in resistivity mode.

Further evidence for the partial rotation of IrMn moments is provided by our Mn *L*-edge X-ray magnetic linear dichroism (XMLD) experiments, characterized by different absorption of light with its linear polarization vector *E* orientated parallel or perpendicular to the spin axis of IrMn. Multilayers of substrate/$[Pt(1)/Co(0.5)]_5$/IrMn/Pt(2) with 6 nm- and 10 nm- thick IrMn were prepared to perform the X-ray absorption experiments since the detection depth is less than 5 nm. The incident angle was fixed at 60°, while the linear polarization of the photon was rotated by 90° to obtain the in-plane (parallel to the easy-direction of IrMn moments) and out-of-plane (60° from the surface) *E*.

Supporting Information

Supporting Information is available from the Wiley Online Library or from the author.

Acknowledgments

The authors acknowledge Beamline BL08U1A in Shanghai Synchrotron Radiation Facility (SSRF) for XAS/XLD measurements and Center for Testing and Analyzing of Materials for technical support. This work was supported by the National Natural Science Foundation of China (Grant Nos. 51322101, 51202125 and 51231004) and National High Technology Research and Development Program of China (Grant no. 2014AA032904 and 2014AA032901).

Received: May 22, 2014
Revised: July 9, 2014
Published online: August 26, 2014

[1] C. Chappert, A. Fert, F. N. V. Dau, *Nat. Mater.* **2007**, *6*, 813.
[2] J. S. Moodera, L. R. Kinder, T. M. Wong, R. Meservey, *Phys. Rev. Lett.* **1995**, *74*, 3273.
[3] J. Moser, A. Matos-Abiague, D. Schuh, W. Wegscheider, J. Fabian, D. Weiss, *Phys. Rev. Lett.* **2007**, *99*, 056601.
[4] P. Li, A. Chen, D. Li, Y. Zhao, S. Zhang, L. Yang, Y. Liu, M. Zhu, H. Zhang, X. Han, *Adv. Mater.* **2014**, *26*, 4320.
[5] F. Pan, S. Gao, C. Chen, C. Song, F. Zeng, *Mater. Sci. Eng. R* **2014**, *83*, 1.
[6] S. Ikeda, K. Miura, H. Yamamoto, K. Mizunuma, H. D. Gan, M. Endo, S. Kanai, J. Hayakawa, F. Matsukura, H. Ohno, *Nat. Mater.* **2010**, *9*, 721.
[7] A. H. MacDonald, M. Tsoi, *Philos. Trans. R. Soc. A* **2011**, *369*, 3098.
[8] S. Loth, S. Baumann, C. P. Lutz, D. M. Eigler, A. J. Heinrich, *Science* **2012**, *335*, 196.
[9] P. Wadley, V. Novák, R. P. Campion, C. Rinaldi, X. Martí, H. Reichlová, J. Železny, J. Gazquez, M. A. Roldan, M. Varela, D. Khalyavin, S. Langridge, D. Kriegner, F. Máca, J. Mašek, R. Bertacco, V. Holy, A. W. Rushforth, K. W. Edmonds, B. L. Gallagher, C. T. Toxon, J. Wunderlich, T. Jungwirth, *Nat. Commun.* **2013**, *4*, 2322.
[10] A. A. Minakov, I. V. Shvets, *Surf. Sci. Lett.* **1990**, *236*, L377.
[11] I. V. Shvets, R. Wiesendanger, D. Bürgler, G. Tarrach, H. J. Güntherodt, J. M. D. Coey, *J. Appl. Phys.* **1992**, *71*, 5489.
[12] Y. Xu, S. Wang, K. Xia, *Phys. Rev. Lett.* **2008**, *100*, 226602.
[13] A. B. Shick, S. Khmelevskyi, O. N. Mryasov, J. Wunderlich, T. Jungwirth, *Phys. Rev. B* **2010**, *81*, 212409.
[14] D. Petti, E. Albisetti, H. Reichlová, J. Gazquez, M. Varela, M. Molina-Ruiz, A. F. Lopeandía, K. Olejník, V. Novák, I. Fina, B. Dkhil, J. Hayakawa, X. Martí, J. Wunderlich, T. Jungwirth, R. Bertacco, *Appl. Phys. Lett.* **2013**, *102*, 192404.
[15] X. Martí, I. Fina, C. Frontera, J. Liu, P. Wadley, Q. He, R. J. Paull, J. D. Clarkson, J. Kudrnovsky, I. Turek, J. Kuneš, D. Yi, J.-H. Chu, C. T. Nelson, L. You, E. Arenholz, S. Salahuddin, J. Fontcuberta, T. Jungwirth, R. Ramesh, *Nat. Mater.* **2014**, *13*, 367.
[16] B. G. Park, J. Wunderlich, X. Martí, V. Holy, Y. Kurosaki, M. Yamada, H. Yamamoto, A. Nishide, J. Hayakawa, H. Takahashi, A. B. Shick, T. Jungwirth, *Nat. Mater.* **2011**, *10*, 347.
[17] Y. Y. Wang, C. Song, B. Cui, G. Y. Wang, F. Zeng, F. Pan, *Phys. Rev. Lett.* **2012**, *109*, 137201.
[18] Y. Y. Wang, C. Song, G. Y. Wang, F. Zeng, F. Pan, *Appl. Phys. Lett.* **2013**, *103*, 202403.
[19] R. Sbiaa, H. Meng, S. N. Piramanayagam, *Phys. Status Solidi RRL* **2011**, *5*, 413.
[20] C. Song, Y. Y. Wang, X. J. Li, G. Y. Wang, F. Pan, *Appl. Phys. Lett.* **2012**, *101*, 062404.
[21] N. A. Pertsev, H. Kohlstedt, *Adv. Funct. Mater.* **2012**, *22*, 4696.
[22] P. He, X. Ma, J. W. Zhang, H. B. Zhao, G. Lüpke, Z. Shi, S. M. Zhou, *Phys. Rev. Lett.* **2013**, *110*, 077203.
[23] T. Yamazaki, Y. Suzuki, T. Katayama, M. Taninaka, K. Nakagawa, A. Itoh, *J. Appl. Phys.* **1991**, *70*, 3180.
[24] S. van Dijken, J. Moritz, J. M. D. Coey, *J. Appl. Phys.* **2005**, *97*, 063907.
[25] T. Nozaki, M. Oida, T. Ashida, N. Shimomura, M. Sahashi, *Appl. Phys. Lett.* **2013**, *103*, 242418.
[26] J. Nogués, I. K. Schuller, *J. Magn. Magn. Mater.* **1999**, *192*, 203.
[27] S. van Dijken, M. Crofton, M. Czapkiewicz, M. Zoladz, T. Stobiecki, *J. Appl. Phys.* **2006**, *99*, 083901.
[28] M. Ali, C. H. Marrows, B. J. Hickey, *Phys. Rev. B* **2003**, *67*, 172405.
[29] Z. Wei, A. Sharma, J. Bass, M. Tsoi, *J. Appl. Phys.* **2009**, *105*, 07D113.
[30] L. Wang, S. G. Wang, S. Rizwan, Q. H. Qin, X. F. Han, *Appl. Phys. Lett.* **2009**, *95*, 152512.
[31] A. Scholl, M. Liberati, E. Arenholz, H. Ohldag, J. Stöhr, *Phys. Rev. Lett.* **2004**, *92*, 247201.
[32] B. Cui, C. Song, F. Li, G. Y. Wang, H. J. Mao, J. J. Peng, F. Zeng, F. Pan, *Sci. Rep.* **2014**, *4*, 4206.
[33] V. Baltz, J. Sort, S. Landis, B. Rodmacq, B. Dieny, *Phys. Rev. Lett.* **2005**, *94*, 117201.

© 2014 WILEY-VCH Verlag GmbH & Co. KGaA, Weinheim